Physicochem. Probl. Miner. Process. 53(2), 2017, 1264−1284

www.minproc.pwr.wroc.pl/journal

Physicochemical Problems of Mineral Processing

ISSN 1643-1049 (print)
ISSN 2084-4735 (online)

Received July 15, 2016; reviewed; accepted May 14, 2017

Energy feature of a multi-flow column flotation process

Gan Cheng[*], Yuexian Yu[**], Liqiang Ma[**], Wencheng Xia[***], Hongxiang Xu[**]

[*] College of Chemistry and Chemical, Henan Polytechnic University, Jiaozuo 454000, Henan, China. Corresponding author: chenggan464@126.com (Gan Cheng)

[**] School of Chemical and Environmental Engineering, China University of Mining and Technology (Beijing), Beijing 100083, China.

[***] School of Chemical Engineering and Technology, China University of Mining and Technology, Xuzhou, China

Abstract: A cyclonic-static micro-bubble flotation column (FCSMC) has been widely used in mineral separation. FCSMC includes countercurrent, cyclone and jet flow mineralization zones in a single column. In this study, the energy feature of the three different zones was compared. The turbulent flow was evaluated in terms of the turbulent kinetic energy (k) and the turbulent dissipation rate (ε). An appropriate computing model was determined by comparing the flow field value measured by PIV with the results of the Fluent numerical simulation. Jet flow separation exhibited the maximum k and ε values among the three columns, whereas counter-current separation displayed the minimum values. The high circulating volumetric flowrate means great energy input and turbulent intensity. The higher turbulent dissipation rate, the smaller the bubble is. The better performance of the FCSMC was mainly attributed to the multiple mineralization steps. The floatability of mineral particles gradually decreases with an increase in flotation time, the mineralization energy gradually increased to overcome the decrease in mineral floatability. By contrast, the countercurrent was beneficial for recovering the coarse particles, and the jet flow was beneficial for recovering the fine particles.

Keywords: *flotation column, turbulent kinetic energy, turbulent dissipation rate, bubble*

Introduction

Working principle of cyclonic-static micro-bubble flotation column

Flotation is an essential fine mineral particles separation technology. Since the flotation column was invented in the mid-1960s, many kinds of flotation columns have sprung up since 1980s (Zhao et al., 2016; Harbort and Clarke, 2017). Among these flotation columns, the cyclonic-static micro-bubble flotation column (FCSMC) introduces the cyclone and jet flow based on traditional counter-current collision mineralization. FCSMC has been developed for nearly three decades and has been

http://dx.doi.org/10.5277/ppmp170245

widely used in various fields (Cheng and Liu, 2015), such as maceral, mineral (e.g., nickel ore, gold ore, fluorite, molybdenite, magnet ore, bauxite, copper, hematite, and lead-zinc ore) and oil-water separation, paper pulp deinking, and waste water treatment. Its structure and separation principle are shown in Fig. 1.

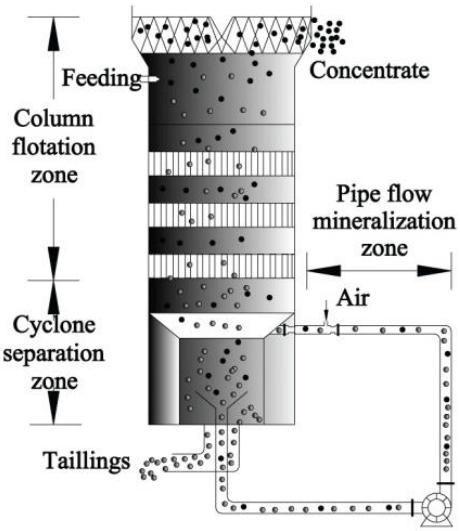

Fig. 1. Separation principle of FCSMC

FCSMC consists of three parts, that is column flotation, cyclone flotation and jet flow flotation units. The column flotation unit features static separation. Counter-current mineralization occurs in this unit. Hydrophobic minerals attached to bubbles are transported into foam layers. Some less hydrophobic particles may undergo attachment and detachment successively and finally fall into the cyclone flotation unit with hydrophilic ones. The cyclone flotation unit acts like a hydrocyclone with the overflow under back pressure. Its drain port is divided into tails port and middling port. When middlings of high velocity circulate through the bubble generator, air is entrained and sheared into abundant microbubbles. This three-phase flow enters the cyclonic reversal cone tangentially. In cyclone flotation unit, mineralized bubble spiral up toward column center and minerals spiral down along wall.

Energy consumption of flotation process

Nothing in the world is permanent, and each change consumes energy (Cheng et al., 2014; Jiang et al., 2016). The energy consumed by ore grinding has been studied and applied widely (Gupta, 2013). The crushing and grinding procedures in the mineral processing of ores constitute a sizable proportion of the total energy, cost, and carbon emission in mining (Drinkwater et al., 2012). Therefore, studies on the energy consumption of flotation process are meaningful (Su et al., 2016; Qin et al., 2016).

Scholars have realized the importance of the energy state of the flotation process. Rinne and Peltola (2008) estimated that the energy consumed by a large mechanical flotation machine throughout its lifetime is approximately two-thirds of the total life-cycle cost of the flotation process. Meanwhile, the initial investment cost was estimated to be approximately 6% of the total life-cycle cost (Lelinski et al., 2011). Thus, energy efficiency and cost influence the overall operating costs of the flotation process the most strongly. Gorain (2012) analyzed the effect of flotation on revenue, operating and capital costs, as well as on environmental and social operation license. Suitable flotation machines and flotation agents effectively reduce the flotation costs. Ragab Fayed (2012) investigated the probabilities of collision, attachment and detachment. They concluded that the turbulent dissipation rate significantly influenced the amount of mineral recovery and the design of flotation devices. Understanding this business component is essential for lowering production costs, increasing earnings and reducing the carbon footprint. Furthermore, several researchers have repeatedly stated that global comminution processes consume between 3 and 4% of the total electrical energy produced in the world (Tromans, 2008). The Australian Federal Government Energy Efficiency Opportunity (EEO) participants in the mining sector consumed 336.5 PJ from 2009 to 2010 (Drinkwater et al., 2012). This value represents approximately 6% of the total energy used in Australia. However, the field of the study of energy consumed by flotation devices is still in its infancy.

Few devices are used to calculate energy both directly and indirectly. Tabosa et al. (2012) used piezoelectric sensors to characterize the degree of velocity fluctuation in a 3 m^3 Metso RCS flotation cell that processes copper sulfide ore. This fluctuation was related to turbulence. This energy rate or specific power input (ε) was proposed to express energy dissipation. This dissipation was in turn related to the net power input (P) of the impeller divided by the total mass of the fluid system (m). Thus, the energy dissipation is expressed as $\varepsilon = P/m$. The overall energy dissipation rate is affected by the cell operation conditions in the following order: impeller speed > impeller size > air flow rate (Tabosa et al., 2012). Researchers have calculated the flotation equipment energy by measuring the motor current (Shen, 2005; Yang et al., 2009). In addition, particle image velocimetry (PIV) (Kong, 2011), particle dynamics analyzer system, laser Doppler velocimetry and computational fluid dynamics (CFD) software (Koh et al., 2003) were used to detect two- or single-phase flow fields in flotation.

Turbulent kinetic energy and turbulent dissipation rate

The turbulent kinetic energy (k) and turbulent dissipation rate (ε) are usually applied to evaluate turbulent flow. The turbulent kinetic energy is used to evaluate the fluctuation of large-scale eddies. The greater the k value is, the higher the fluctuating velocity is. The turbulent kinetic energy is defined as follows (Wang et al., 2017):

$$k = \frac{1}{2}(\overline{v_i' v_i'}) = \frac{1}{2}(v_x'^2 + v_y'^2 + v_z'^2) \tag{1}$$

where v_i' is the fluctuating velocity and *x*, *y*, and *z* are the axial, radial and tangential axes, respectively.

The turbulent dissipation rate is defined as the lost turbulent kinetic energy per unit mass fluid per unit time, which is given as follows:

$$\varepsilon = \frac{\mu}{\rho}\left(\frac{\partial v_x'}{\partial v_y'}\right)\left(\frac{\partial v_x'}{\partial v_y'}\right) \tag{2}$$

where μ is the dynamic viscosity and ρ is the density.

A dimensional consideration of the determination of the energy dissipation is used by Hinze (1975):

$$\varepsilon = 15\frac{\mu}{\rho}\cdot\frac{v'^2}{\lambda} \tag{3}$$

where λ is the microscopic turbulence length scale. The turbulence fluctuating velocity in the main flow direction is given by *v*' (Hlawitschka and Bart, 2012).

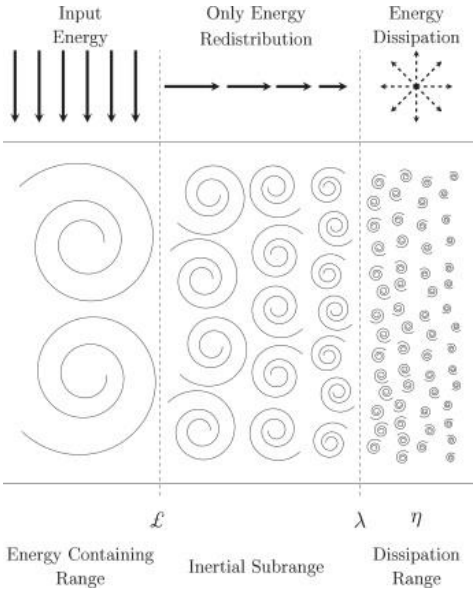

Fig. 2. Diagram representing energy cascade process in a fully developed turbulence. The energy input occurs by large eddies, is redistributed through inertial subrange and is dissipated for the small eddies

Figure 2 presents a diagram showing how the energy transfer process occurs across the motion scales. A cascade process happens in which the largest eddies give rise to smaller eddies, and these eddies to even smaller eddies, until the dissipative scales,

where the turbulent kinetic energy becomes heat. The microscopic turbulence length scale is formulated in terms of k and ε (Puhales et al., 2015):

$$\lambda = \left(\frac{\nu k}{\varepsilon} \right)^{1/2} \tag{4}$$

where ν is the kinematic viscosity.

Kolmogorov (1941) derived a formula for the energy spectrum of turbulence, which described the distribution of energy among turbulence vortices as a function of vortex size. He described how the energy is transferred from larger to smaller eddies, how much energy is contained by eddies of a given size and how much energy is dissipated by eddies of each size. Two hypothesis were proposed. Kolmogorov's 1st hypothesis was: the smallest scales receive energy at a rate proportional to the dissipation of energy rate; motion of the very smallest scales in a flow depend on rate of energy transfer from small scales and kinematic viscosity. Kolmogorov's 2st hypothesis was: in Turbulent flow, a range of scales exists at very high *Re* where statistics of motion in a range have a universal form that is determined by dissipation and independent of kinematic viscosity.

Wu and Patterson (1989) found that in the outflow of a given impeller Eulerian macro length scales are independent of operating conditions (impeller speed). Deviations between the experimentally observed (Wu and Patterson, 1989) and simulated radial profiles of Eulerian macro length scales normalized with the impeller blade height were given by Jenne and Reuss (1999).

Bubble is the core of the flotation process, and a bubble size governs the surface area over which solid particles and bubbles interact and contribute significantly to system hydrodynamics, which affects the process performance. Many factors affect the bubble size, including the superficial gas velocity, frother type and concentration, bubble-generation device and operating pressure. This study mainly investigates and analyzes the effect of the energy feature on the bubble-size distribution.

In this study, the energy feature of the three different zones of FCSMC were described and compared. The energy feature was evaluated in terms of the turbulent kinetic energy (k) and turbulent dissipation rate (ε).

Experimental method and procedure

Fundamental equation

Mass conservation and momentum conservation equations must be employed for numerical simulation. Mass conservation equations are also known as continuity equations. The integral form is written as follows:

$$\frac{\partial}{\partial t}\iiint_{Vol}\rho dxdydz+\iint_{A}\rho dA=0 \tag{5}$$

where, *Vol* is the control volume and *A* is the control surface.

The differential form of Equation (5) in the Cartesian coordinate system is expressed by:

$$\frac{\partial\rho}{\partial t}+\frac{\partial(\rho v_x)}{\partial x}+\frac{\partial(\rho v_y)}{\partial y}+\frac{\partial(\rho v_z)}{\partial z}=0\,. \tag{6}$$

For the steady incompressible flow, the density ρ is constant, and thus Equation (6) becomes:

$$\frac{\partial v_x}{\partial x}+\frac{\partial v_y}{\partial y}+\frac{\partial v_z}{\partial z}=0\,. \tag{7}$$

Momentum conservation equations are also known as either motion or Navier-Stokes equations. The equations for three directions *x*, *y*, and *z* are expressed as follows:

$$\begin{aligned}
&\frac{\partial(\rho v_x)}{\partial t}+div(\rho v_x\overline{v}_x)=div(\mu gradv_x)-\frac{\partial\rho}{\partial x}+S_u\\
&\frac{\partial(\rho v_y)}{\partial t}+div(\rho v_y\overline{v}_y)=div(\mu gradv_y)-\frac{\partial\rho}{\partial y}+S_v\\
&\frac{\partial(\rho v_z)}{\partial t}+div(\rho v_z\overline{v}_z)=div(\mu gradv_z)-\frac{\partial\rho}{\partial z}+S_w
\end{aligned} \tag{8}$$

where $grad\,()=\partial()/\partial x+\partial()/\partial y+\partial()/\partial z$ and S_u, S_v, and S_v represent the generalized source.

Simulation objects

The structure and size charts (in mm) of the three flotation columns are illustrated in Fig. 3. The column height and diameter were set at 650 and 100 mm, respectively. The height/diameter ratio was 6.5, which satisfied the requirements presented in the literature (Yianatos, 1989). Tests were conducted with deionized water and a tailing device was not set. A circulating volumetric flowrate was adjusted using a pump outlet valve.

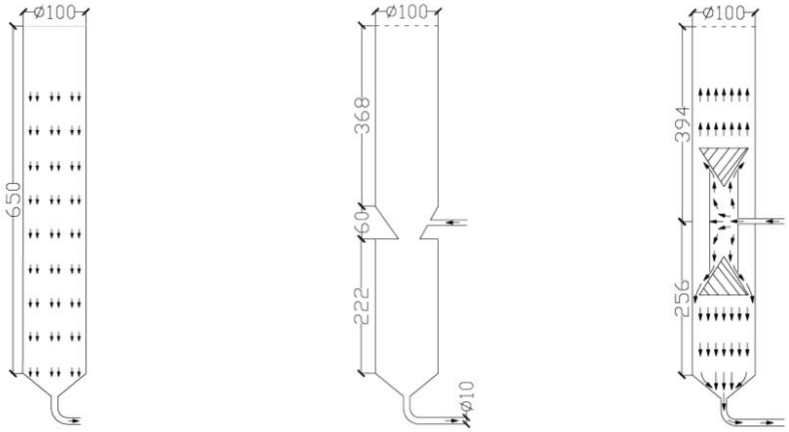

(a) counter-current flotation column (b) cyclone flotation column (c) jet flow flotation column

Fig. 3. Structure and size charts (in mm) of three flotation columns

Meshing

The computational models were constructed using UG 6.0 software (Siemens, Germany), and meshing was completed with Gambit 2.4.6 (fluent pre-processing software, ANSYS Inc., America). Structured and unstructured hybrid grids were considered. The upper surface of the flotation columns was set at Z=0 plane, and the centre of the plane was the coordinate origin. Unless stated otherwise, SI units were used in the numerical simulation.

The skewness of a grid was an apt indicator of the mesh quality and suitability. Large skewness compromised the accuracy of the interpolated regions. The grid number and skewness of the counter-current were 132,090 and 0.70, respectively; those of the cyclone were 346,370 and 0.70, respectively; and those of jet flow were 149,480 and 0.75, respectively. These values satisfied the skewness requirement for a value of less than 0.9 (Huang, 2013).

Boundary conditions

The flotation process simulation is complex. Upon considering the computational accuracy and computing power, the boundary conditions were set as follows:

1) fluid was assumed to flow in a single phase, namely, the liquid phase (water)

2) the entire process involved the isothermal flow and no heat was transmitted

3) the fluid was incompressible

4) a no-slip boundary condition was imposed on all of the walls, that is, all velocity components were zero. The standard wall function was adopted in the calculation of the near-wall region

5) the value of the pressure outlet was set as the atmospheric pressure. The pressure outlet referred to the top of flotation column.

The physical parameters of water are presented in Table 1.

Table 1. Physical parameters of water

Density	Gravitational acceleration	Thermal conductivity
998.2 kg/m^3	-9.80 m/s^2	0.6 W/(m·K)
Kinetic coefficient of viscosity	Specific heat capacity	
1.003×10^{-3} kg/(m·s)	4.182×10^{3} J/(kg·K)	

Computational modeling

Pressure-velocity coupling was calculated using the SIMPLE algorithm. The discrete solutions of discrete pressure, momentum and turbulence equations were obtained using the least square method, second-order upwind and first-order upwind, respectively (Wei et al., 2017). To determine the suitability of the model for calculating the internal flow field of the flotation columns, PIV was applied to detect the flow field. An appropriate computing model was determined by comparing the PIV flow field measured value and the Fluent numerical simulation results.

PIV flow field measurement system and method

PIV is a well-established technique for measuring the velocity fields in fluid systems (Wang and Ergin, 2014). A Dantec Dynamics PIV system was used to measure the velocity. This system is composed of a double pulse laser, two Nikkor 60-mm lenses, a Timerbox for synchronization and DynamicStudio software to control overall measurement. The specific parameters are listed in Table 2, and the test platform for the PIV flow field is shown in Fig. 4.

Table 2. Main equipment of PIV flow field test system

Equipment	Model and parameter	Manufacturer	Function
Laser device	Solo 200 XT Nd: YAG, 200 mJ, 15 Hz	New Wave Research	Double pulse laser
CCD camera	FlowSense EO 4M	Dantec Dynamics	Acquisition of flow field information
Synchronous controller	Timer Box	New Wave Research	To ensure the synchronization of laser and camera
Analysis software of flow field	Dynamic Studio-v3.20	Dantec Dynamics	Post-processing of flow field
Circulating pump	Self-priming vortex, Power: 370 W, Capacity: 1 m^3/h	Shanghai Xinhu Electric machine Co., TLD	Energy supply

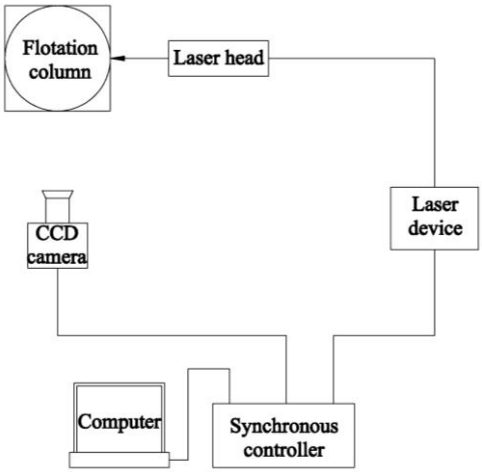

Fig. 4. Sketch map of PIV flow field test platform

Results and discussion

Comparison of PIV measured value and value from Fluent simulation

An appropriate computing model is determined by comparing the measured value for the PIV flow field with the results of the Fluent numerical simulation. The circulating volumetric flowrate is set at 0.413 m^3/h.

For the counter-current flotation column, the Y=0 plane is selected as the measuring surface. For the cyclone flotation column, the cyclone inlet plane is selected as the measuring surface. For the jet flow flotation column, the jet flow section is selected as the measuring surface. The comparative results of Fluent numerical simulation and PIV measured value are displayed in Figs. 5, 6 and 7.

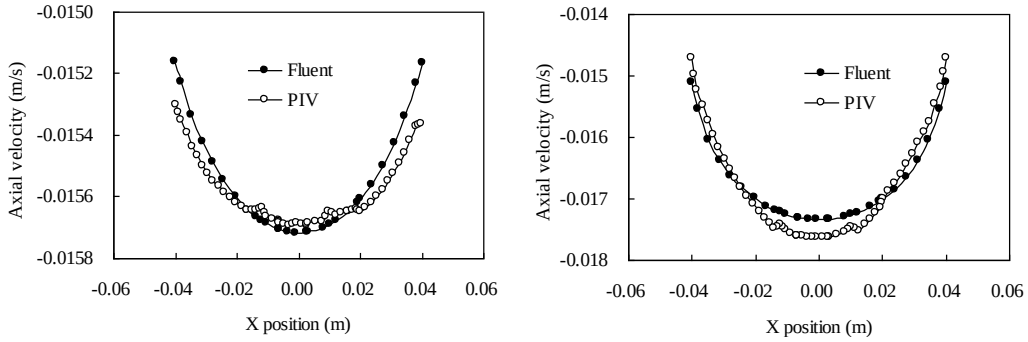

(a) Z = -0.20 m (b) Z = -0.50 m

Fig. 5. Comparison of the PIV measured value and the value from the Fluent simulation (counter-current flotation column)

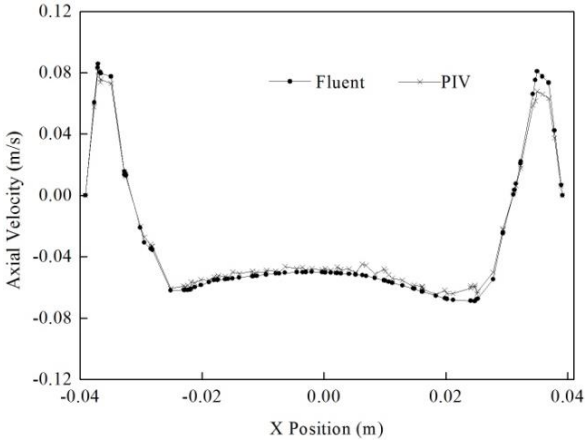

Fig. 6. Comparison of the PIV measured value and the value from the Fluent simulation (cyclone flotation column)

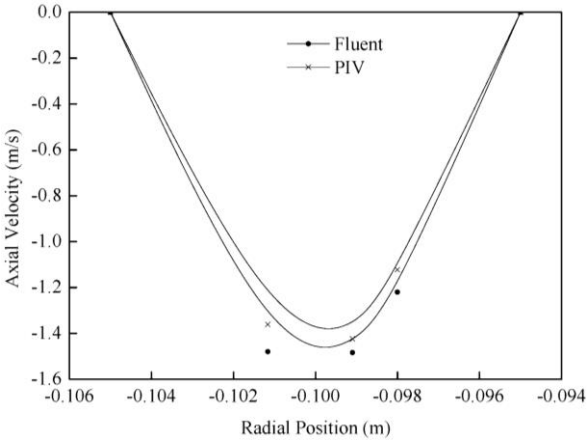

Fig. 7. Comparison of the PIV measured value and the value from the Fluent simulation (jet flow flotation column)

Figures 5, 6 and 7 suggest that the variation trend between the measured value for the flow field and the numerically simulated value is consistent. Nonetheless, these values differ because the flow field obtained through numerical simulation is ideal whereas the actual process of fluid flow is affected by multiple factors. Thus, a consensus between the measurement and the simulation is difficult to reach. Therefore, the computational model adopted in numerical simulation can describe the flow field distribution within flotation columns.

Turbulent energy feature of counter-current flotation column

The turbulent energy is adjusted by changing the circulating volumetric flowrate. The selected circulating volumetric flowrates are 0.253, 0.295, 0.342, 0.387, 0.413, 0.446,

0.467, and 0.495 m^3/h, among which five levels are analysed. The turbulent kinetic energy in the $Y = 0$ plane under different circulating volumetric flowrates is shown in Fig. 8.

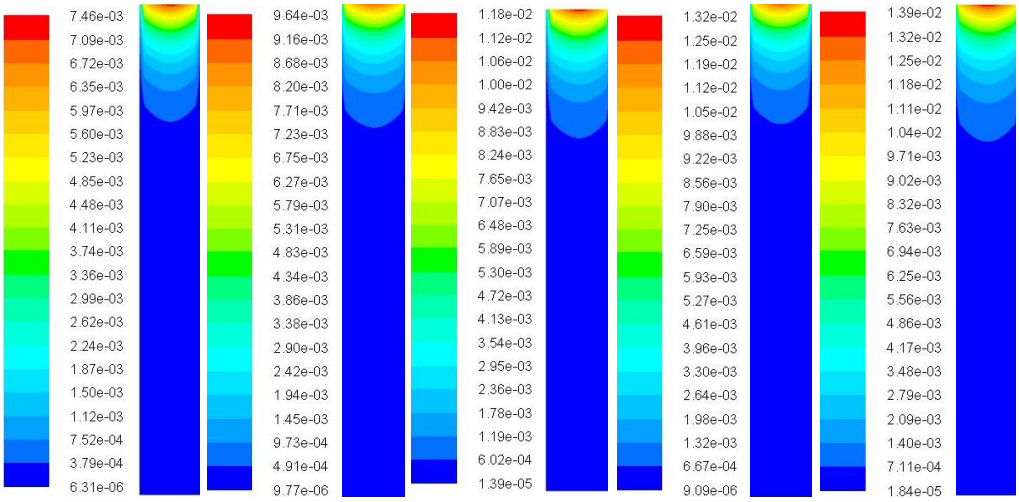

(a) 0.253 m^3/h (b) 0.342 m^3/h (c) 0.413 m^3/h (d) 0.467 m^3/h (e) 0.495 m^3/h

Fig. 8. Effect of circulating volumetric flowrate on turbulent kinetic energy

Figure 8 shows that k value is maximized in the feeding inlet and that this value increases with an increase in the circulating volumetric flowrate. When the circulating volumetric flowrate increases from 0.253 to 0.495 m^3/h, the maximum k value increases from 7.46×10^{-3} to 1.39×10^{-2} m^2/s^2.

The turbulent dissipation rate in the $Y = 0$ plane under different circulating volumetric flowrates are depicted in Fig. 9. The ε value increases with an increase in the circulating volumetric flowrate. When the circulating volumetric flowrate increases from 0.253 to 0.495 m^3/h, the maximum ε value increases from 1.75×10^{-2} to 4.54×10^{-2} m^2/s^3.

Figure 10 shows the mean k and ε values of the counter-current flotation column for different circulating volumetric flowrates. Both k and ε increase with an increase in the circulating volumetric flowrate. When the circulating volumetric flowrate increases from 0.253 to 0.495 m^3/h, the mean k value increases from 4.28×10^{-4} to 9.19×10^{-4} m^2/s^2 and the mean ε value increases from 3.14×10^{-4} to 8.98×10^{-4} m^2/s^3.

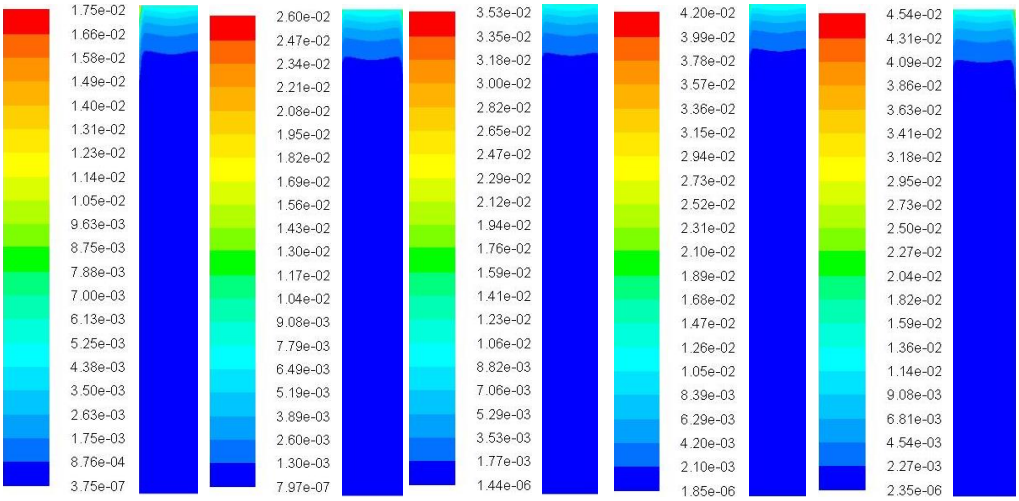

(a) 0.253 m^3/h (b) 0.342 m^3/h (c) 0.413 m^3/h (d) 0.467 m^3/h (e) 0.495 m^3/h

Fig. 9. Effect of circulating volumetric flowrate on turbulent dissipation rate

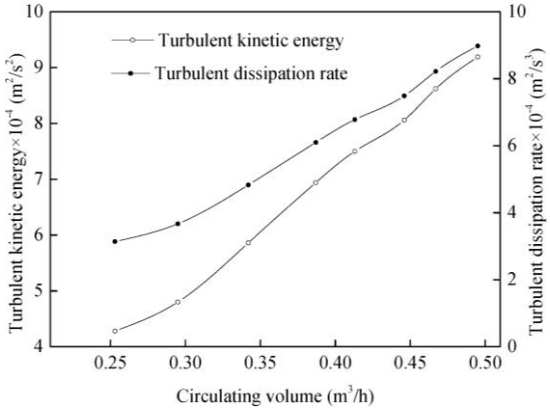

Fig. 10. Mean k and ε values of counter-current flotation column under different circulating volumetric flowrates

Turbulent energy feature of cyclone flotation column

The selected circulating volumetric flowrates are 0.253, 0.295, 0.342, 0.387, 0.413, 0.446, 0.467, and 0.495 m^3/h. The turbulent kinetic energy and turbulent dissipation rate of the feeding inlet plane of the cyclone under different circulating volumetric flowrates are shown in Figs. 11 and 12. The maximum and minimum values of k and ε differ considerably. Thus, a full-range display cannot reflect changes. The maximum k value is set at 4×10^{-3} m^2/s^2, and the maximum ε value is set at 0.5 m^2/s^3.

As indicated in Fig. 11, the k value is maximized at the largest radius. The relatively high k region increases in the size with an increase in the circulating volumetric flowrate.

Figure 12 suggests that the ε value is maximized at the largest radius. The relatively high ε region increases in the size with an increase in the circulating volumetric flowrate.

The mean k and ε values of the cyclone segment under different circulating volumetric flowrates are provided in Fig. 13.

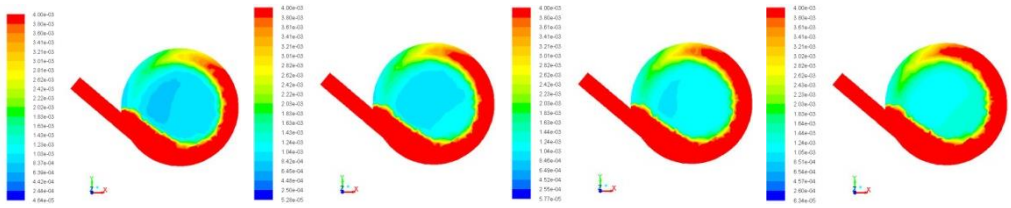

(e) 0.413 m^3/h (f) 0.446 m^3/h (g) 0.467 m^3/h (h) 0.495 m^3/h

Fig. 11. Turbulent kinetic energy of feeding inlet plane of cyclone under different circulating volumetric flowrates

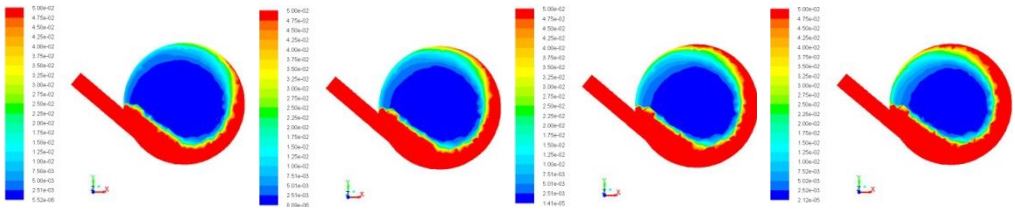

(a) 0.253 m^3/h (b) 0.295 m^3/h (c) 0.342 m^3/h (d) 0.387 m^3/h

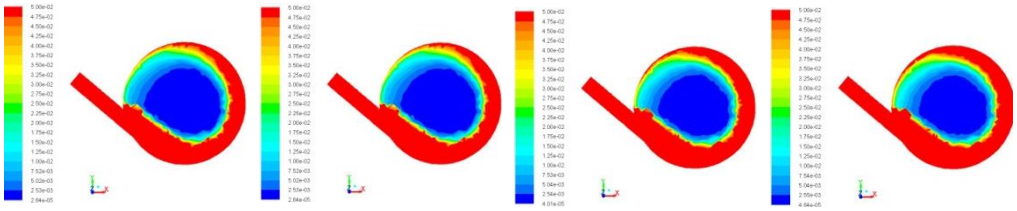

(e) 0.413 m^3/h (f) 0.446 m^3/h (g) 0.467 m^3/h (h) 0.495 m^3/h

Fig. 12. Tturbulent dissipation rate of feeding inlet plane of cyclone under different circulating volumetric flowrates

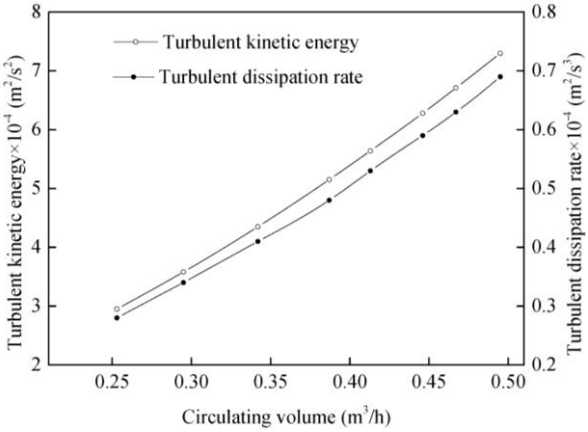

Fig. 13. Mean k and ε values of cyclone segment under different circulating volumetric flowrates

The mean k and ε values increase with an increase in the circulating volumetric flowrate. When the circulating volumetric flowrate increases from 0.253 to 0.495 m^3/h, the mean k value increases from 2.95×10^{-3} to 7.30×10^{-3} m^2/s^2 and the mean ε value increases from 0.28 to 0.69 m^2/s^3. An increase in k improves the fluctuating velocity of particles and fine particles can be recovered. However, this increase enhances the probability of coarse particle detachment.

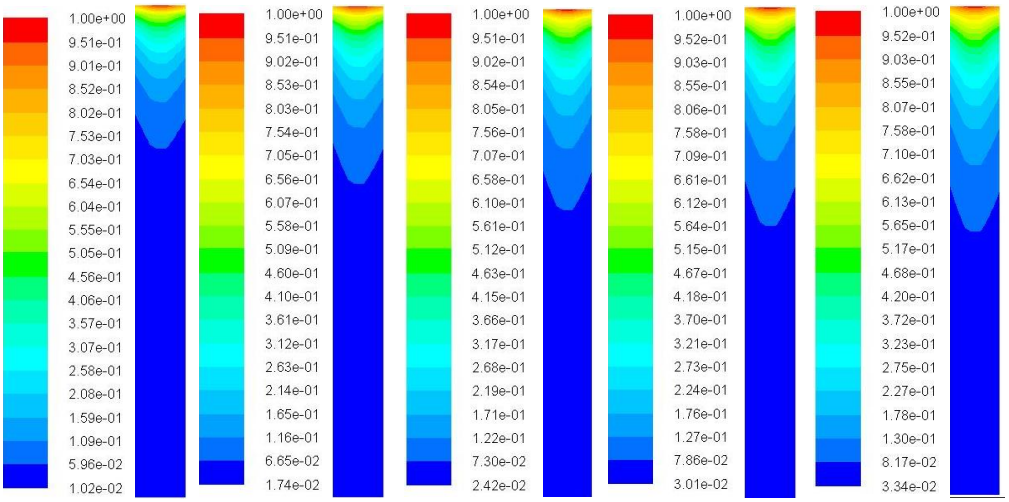

(a) 0.253 m^3/h (b) 0.342 m^3/h (c) 0.413 m^3/h (d) 0.467 m^3/h (e) 0.495 m^3/h

Fig. 14. Turbulent kinetic energy in $Y = 0$ plane under different circulating volumetric flowrates

Turbulent energy feature of jet flow flotation column

The selected circulating volumetric flowrates are 0.253, 0.295, 0.342, 0.387, 0.413, 0.446, 0.467 and 0.495 m^3/h, among which five levels are analyzed. The turbulent kinetic energy in the $Y = 0$ plane for different circulating volumetric flowrates is shown in Fig. 14. The k value is maximized in the feeding inlet of jet flow. This value increases with an increase in circulating volumetric flowrate, along with the size of the relatively high k region.

The turbulent kinetic dissipation rate in the $Y = 0$ plane for different circulating volumes is depicted in Fig. 15. The ε value is maximized in the feeding inlet of the jet flow. This value increases with an increase in the circulating volumetric flowrate, along with the size of the relatively high turbulent kinetic dissipation rate region.

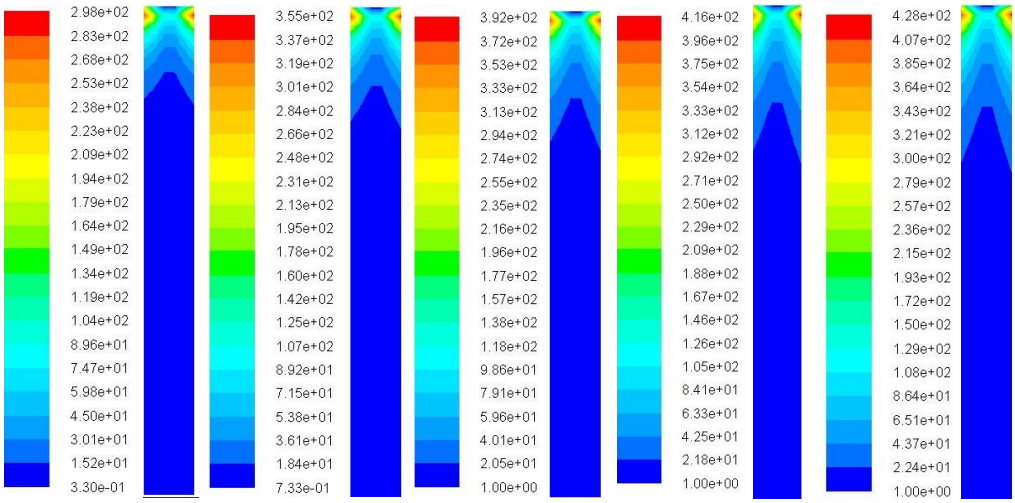

(a) 0.253 m^3/h (b) 0.342 m^3/h (c) 0.413 m^3/h (d) 0.467 m^3/h (e) 0.495 m^3/h

Fig. 15. Effect of middling circulating volumetric flowrates on turbulent dissipation rate of $Y = 0$ plane

The mean k and ε values of a jet flow segment under different circulating volumetric flowrates are provided in Fig. 16. The mean k and ε values increase with an increase in the circulating volumetric flowrate. When the circulating volumetric flowrate increases from 0.253 to 0.495 m^3/h, the mean k value increases from 0.077 to 0.144 m^2/s^2 and the mean ε value increases from 9.33 to 19.42 m^2/s^3. The k and ε values of jet flow are the highest among the three separation methods. Particles and air bubbles collide in a small jet flow space, the significance of collision frequency increases and the collision probability increases. Meanwhile, an increased amount of turbulent kinetic energy enhances the probability of coarse particle detachment.

The mean k and ε values increase with an increase in the circulating volumetric flowrate. When the circulating volumetric flowrate increases from 0.253 to 0.495 m^3/h,

the mean k value increases from 0.077 to 0.144 m^2/s^2 and the mean ε value increases from 9.33 to 19.42 m^2/s^3. The k and ε values of jet flow are the highest among the three separation methods. The particles and air bubbles collide in a small jet flow space, the significance of collision frequency increases and the collision probability increases. Meanwhile, an increased amount of turbulent kinetic energy enhances the probability of coarse particle detachment.

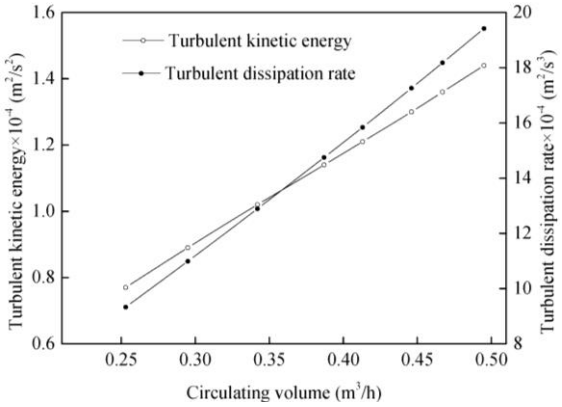

Fig. 16. Mean k and ε values of a jet flow segment under different circulating volumetric flowrates

Comparison of turbulent energies

Table 3 presents the result of the comparison between the k and ε values of the three separation processes for different circulating volumetric flowrates.

Table 3. Comparison between the k and ε values of three separation processes for different circulating volumetric flowrates

Separation process	Counter-current	Cyclone	Jet flow
k value (m^2/s^2)	0.0004~0.0009	0.002~0.008	0.07~0.15
ε value (m^2/s^3)	0.0003~0.0009	0.2~0.7	9~20

The data given in Table 3 suggest that the k and ε values of jet flow are the highest among the three processes, whereas those of counter-current are the lowest. The k value of the jet flow is 20 to 26 times that of the cyclone and 150 to 180 times that of the counter-current. Moreover, the ε value of jet flow is 28 to 34 times that of the cyclone and 20000 to 30000 times that of the counter-current. According to the difference in the turbulent energy, the three separation processes can be described as follows: low-turbulence counter-current separation, medium-turbulence cyclone separation, and high-turbulence jet flow.

Micro eddy size is expressed as follows:

$$l_D = (v^3 / \varepsilon)^{1/4} \tag{9}$$

where v is the kinetic viscosity (m^2/s), and the viscosity of water is 1.005×10^{-6} m^2/s; ε is the turbulent dissipation rate (W/kg or m^2/s^3). In Equation (9) the eddy size is related to the turbulent dissipation rate. The greater the dissipation rate is, the smaller the eddy is. The eddy size of the three separation processes is listed in Fig. 17. Figure 17 shows that eddy size decreases approximately in line with an increase in ε. The eddy size range of the counter-current is from 180 to 240 μm, that of the cyclone is from 30 to 40 μm, and that of jet flow is from 15 to 18 μm.

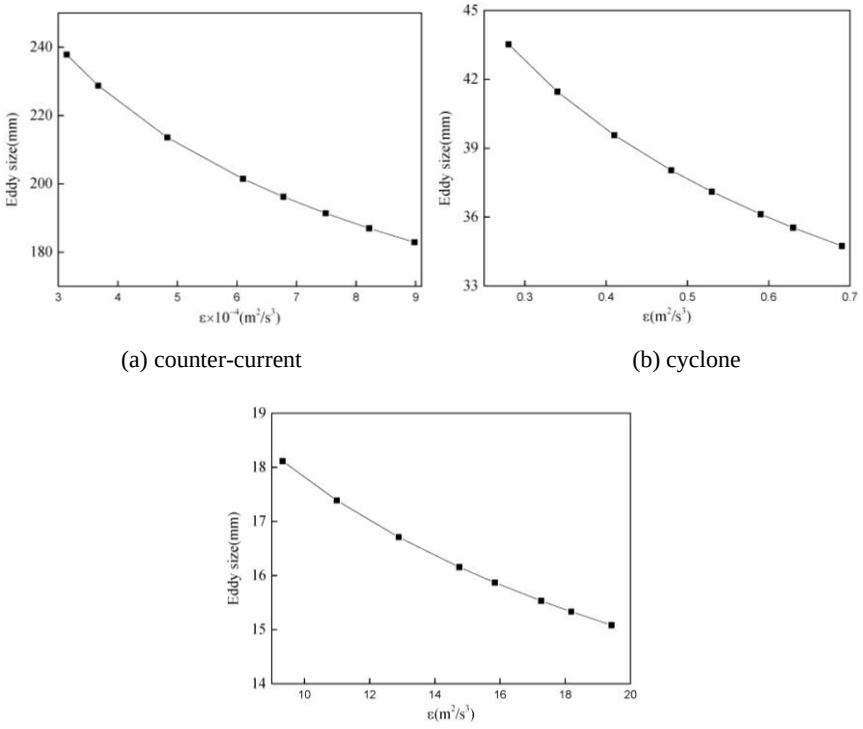

(a) counter-current (b) cyclone

(c) jet flow

Fig. 17. Relationship between eddy size and ε

Bubble size comparison

The bubble size comparison has been conducted elsewhere (Cheng et al., 2016). Figure 18 shows that the bubble size decreases as the circulating volume increases in the three separation processes. Under the same circulating rate, the bubble diameter of the countercurrent flotation column is maximum and that of the jet flow flotation column is minimum. Their turbulent dissipation rate is different and affects the bubble size and flotation effect. Comparing the turbulent dissipation rate, the jet flow is maximum and the countercurrent is minimum. Therefore, the higher turbulent dissipation rate, the smaller the bubble is.

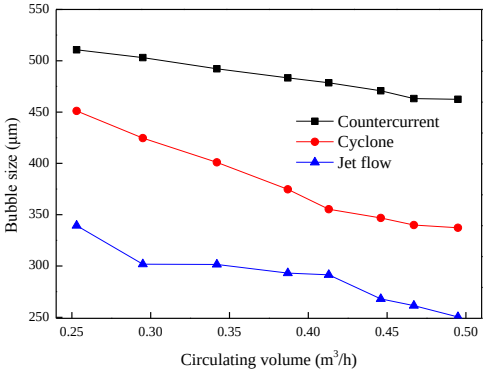

Fig. 18. Effect of different flotation columns on bubble sizes

Comparison of flotation behavior

As previously mentioned, many flotation tests were conducted based on FCSMC. As can be seen from Fig. 19, the grade and recovery of P_2O_5 concentrate increased with the circulation pressure from 0.18 to 0.24 Mpa. The high efficiency mineralization can be attributed to the increase in energy introduced in the system through the enhanced circulation pressure. The comparison of the three separation processes is shown in Fig. 20. The detailed content will be published subsequently. As shown in Fig. 20, when the combustible recovery was similar, the concentrate ash of the countercurrent was minimum, whereas that of the jet flow was maximum. The finer the particle size, the worse the floatability was. By contrast, the countercurrent was beneficial for recovering the coarse particles and the jet flow was beneficial for recovering the fine particles.

Table 4. Comparison of industrial systems between FCSMC and BF mechanical flotation cell for magnetite ore separation (Zhang et al., 2013)

Industrial separation system	Fe(%)			Fe Rec (%)	Power consumption per ton (kW h/t)	Flowsheet
	Feed	Conc.	Tailings			
BF mechanical flotation cell	63.59	69.23	26.37	94.54	6.85	One rougher two scavenger and magnetic separation process
FCSMC flotation column	63.59	69.15	22.37	95.82	6.12	One rougher one cleaner magnetic separation and grinding process

From Table 4, we can see that the effect of FCSMC is superior to BF. The FCSMC integrates with three parts, that is the column flotation, cyclone flotation and jet flow flotation units. The better performance of FCSMC was mainly attributed to the multiple mineralization steps. The floatability of mineral particles gradually decreases with an increase in flotation time, the mineralization energy gradually increased to overcome the decrease in mineral floatability.

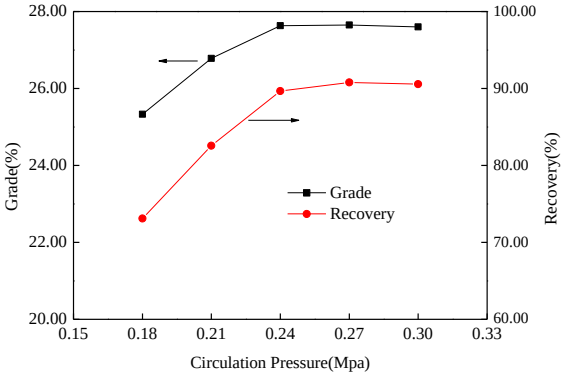

Fig.19. P_2O_5 grade and recovery at different circulation pressures conducted in FCSMC flotation column (Li et al., 2012). Pressures were adjusted between 0.18 and 0.30 Mpa. High circulation pressure means great circulating volumetric flowrate and strong energy input

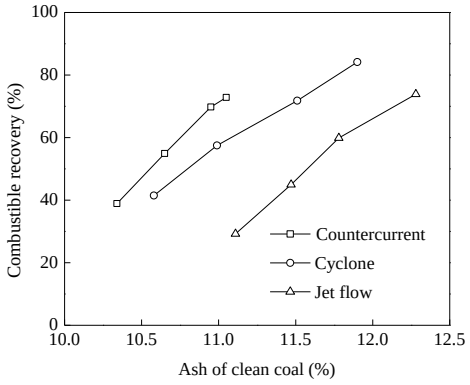

Fig. 20. Comparison of concentrate ash and combustible recovery of three separation processes

Conclusions

The turbulent energy is important in a flotation process. The turbulent kinetic energy (k) and turbulent dissipation rate (ε) are typically used to evaluate the turbulent flow. This study generated much data in this respect, and the conclusions drawn based on these data are summarized as follows.

The k and ε values of jet flow were the highest among the three flotation columns, whereas those of counter-current were the lowest. According to the differences in turbulent energies, the three separation processes can be described as follows: low-turbulence counter-current separation, medium-turbulence cyclone separation and high-turbulence jet flow.

The high circulating volumetric flowrate means great energy input and turbulent intensity. A better performance of FCSMC was mainly attributed to the multiple mineralization steps. Floatability of mineral particles gradually decreased with an

increase in flotation time, the mineralization energy gradually increased to overcome the decrease in mineral floatability. By contrast, the countercurrent was beneficial for recovering the coarse particles and the jet flow was beneficial for recovering the fine particles.

Acknowledgements

The Authors would like to thank the support from "National Natural Science Foundation of China" (Grant No. 51604097),"China Postdoctoral Science Foundation" (Grant No. 172524), "Henan Postdoctoral Science Foundation" (Grant No. 172524), "Key project of science and technology research of Education Department of Henan Province" (Grant No. 16A440002), and "Key project of science and technology research of Education Department of Henan Province" (Grant No. 17B440003).

References

CHENG G., LIU J.T., 2015. *Development of Column Flotation Technology*. J. Chem. Pharm. Res., 7(2):540-549.

CHENG G., LIU J.T., MA L.Q., CAO Y.J., LI J.H., HUANG G., 2014. S*tudy on Energy Consumption in Fine Coal Flotation*. Int. J. Coal Prep. Util., 34(1): 38-48.

CHENG G., SHI C.L., LIU J.T., YAN X.K., 2016. *Bubble-Distribution Measurement in a Flotation Column*. Int. J. Coal Prep. Util., 36(5): 241-250.

DRINKWATER D., NAPIER-MUNN T., BALLANTYNE G., 2012. *Energy reduction through eco-efficient comminution strategies*. 26th International Mineral Processing Congress. New Delhi: 1223-1229.

GORAIN B.K., 2012. *Developing solutions to complex flotation problems*. 26th International Mineral Processing Congress. New Delhi: 1657-1675.

GUPTA V.K., 2013. *Validation of an energy–size relationship obtained from a similarity solution to the batch grinding equation*. Powder Technol., 249: 396-402.

HARBORT G., CLARKE D., 2017. *Fluctuations in the popularity and usage of flotation columns -An overview*. Miner. Eng., 100: 17-30.

HINZE J.O., 1975. *Turbulence*. McGraw-Hill, New York.

HLAWITSCHKA M.W., BART H.J., 2012. *Determination of local velocity, energy dissipation and phase fraction with LIF and PIV-measurement in a Kühni miniplant extraction column.* Chem. Eng. Sci., 69(1): 138-145.

HUANG G., 2013. *Interfacial Effects of Flotation Conditioning and Process Intensification*. China University of Mining and Technology, China.

JEANNE M., REUSS M., 1999. *A critical assessment on the use of k–ε turbulence models for simulation of the turbulent liquid flow induced by a Rushton-turbine in baffled stirred-tank reactors*. Chem. Eng. Sci., 54: 3921-3941.

JIANG H.J., CAO S.G., ZHANG Y., WANG C.. 2016. *Analytical solutions of hard roof's bending moment, deflection and energy under the front abutment pressure before periodic weighting*. International Journal of Mining Science and Technology 26(1): 175-181.

KOH P.T.L., SCHWARZ M.P., ZHU Y., BOURKE P., PEAKER R., FRANZIDIS J.P., 2003. *Development of CFD models of mineral flotation cells*. Third International Conference on CFD in the Minerals and Process Industries. Melbourne: 171-175.

KOLMOGOROV, A.N., 1941. *The local structure of turbulence in incompressible viscous fluid for very large Reynolds numbers*. Proc. USSR Acad. of Sci., 30: 299-303.

KONG L.T., 2011. *Study and Measure on Cyclonic Flow Field of Floatation Column by the PIV*. China University of Mining and Technology, China.

LELINSKI D., GOVENDER D., DABROWSKI B., TRACZYK F., MULLIGAN M., 2011. *Effective use of energy in the flotation Process*. 6th Southern African Base Metals Conference. Phalaborwa: 137-148.

LI G.S., CAO Y.J., LIU J.T., WANG D.P., 2012. *Cyclonic flotation column of siliceous phosphate ore*. Int. J. Miner. Process., 110-111: 6-11.

PUHALES F. S., DEMARCO G., MARTINS L.G.N., ACEVEDO O.C., DEGRAZIA G. A., WELTER G. S., COSTA F. D., FISCH G. F., AVELARD A.C., 2015. *Estimates of turbulent kinetic energy dissipation rate for a stratified flow in a wind tunnel*. Physica A 431: 175-187.

QIN Z. H., LI X., SUN H., ZHAO C. C., RONG L. M., 2016. *Caking property and active components of coal based on group component separation*. International Journal of Mining Science and Technology 26: 571-575.

RAGAB S.A., FAYED H., 2012. *Collision frequency of particles and bubbles suspended in homogeneous isotropic turbulence*. 50th AIAA Aerospace Sciences Meeting Including the New Horizons Forum and Aerospace Exposition. Nashville: 1-12.

RINNE A., PELTOLA A., 2008. *On lifetime costs of flotation operations*. Miner. Eng., 21(12-14): 846-850.

SHEN Z.C., 2005. *Research of 160 m^3 flotation machine flotation dynamics*. Nonferrous Met. (Miner. Process. Sect.), 27(5): 33-35.

SU X. B., SI Q., WANG Q., 2016. *The XRD response during the coalification process*. Journal of Henan Polytechnic University (Natural Science), 35: 487-492.

TABOSA E., RUNGE K., HOLTHAM P.N., 2012. *Development and application of a technique for evaluating turbulence in a flotation cell*. 26th International Mineral Processing Congress. New Delhi: 5377-5390.

TROMANS D., 2008. *Mineral comminution: Energy efficiency considerations*. Miner. Eng., 21(8): 613-620.

WANG F.J., 2004. *Computational fluid dynamics analysis-Principles and Applications of CFD software*. Tsinghua University Press, China.

WANG L.J., WANG Y.H., YAN X.K., WANG A., CAO Y.J., 2017. *A numerical study on efficient recovery of fine-grained minerals with vortex generators in pipe flow unit of a cyclonic-static micro bubble flotation column*. Chem. Eng. Sci., 158: 304-313.

WEI L.B., LI D.H., CHEN Z.G., SUN M.Y., ZHU X.S., 2017. *Numerical simulation of force and separation on particles in pulsing airflow*. Journal of China University of Mining & Technology 46(1): 162-168+176.

YANG L.J., SHI S.X., CHEN D., DONG G.G., ZHANG Y.J., LAI M.H., 2009. *Research of 200 m^3 flotation machine flotation dynamics*. Nonferrous Met. (Miner. Process. Sect.), 31(2): 29-31.

YIANATOS J.B., 1989. *Column Flotation Modelling and Technology*. International Colloquium-Developments in Froth Flotation. Cape Town: 1-30.

ZHANG H.J., LIU J.T., WANG Y.T., CAO Y.J., MA Z.L., LI X.B., 2013. *Cyclonic-static micro-bubble flotation column*. Miner. Eng. 45: 1-3.

ZHAO D. F., GUO Y. H., BAI W. B., ZHANG J. X., LI M., GUO, X. Y., 2016. *The characteristics and influencing factors of nanopores in shale gas reservoir of Wufeng and Longmaxi formation in southeast Chongqing*. Journal of Henan Polytechnic University (Natural Science), 35: 497-506.